Establishing the timings of individual rainfall-triggered landslides using Sentinel-1 satellite radar data

Katy Burrows[1], Odin Marc[1], and Dominique Remy[1]

[1]Géoscience Environnement Toulouse, Toulouse, France

Correspondence: Katy Burrows (katy.burrows@get.omp.eu)

Abstract. Heavy rainfall events in mountainous areas can trigger thousands of destructive landslides, which pose a risk to people and infrastructure and significantly affect the landscape. Landslide locations are typically mapped using optical satellite imagery, but in some regions their timings are often poorly constrained due to persistent cloud cover. Physical and empirical models that provide insights on the processes behind the triggered landsliding require information on both the spatial extent and timing of landslides. Here we demonstrate that Sentinel-1 SAR amplitude time series can be used to constrain landslide timing to within a few days and present three methods to accomplish this based on time series of: (i) the difference in amplitude between the landslide and its surroundings, (ii) the spatial variability of amplitude between pixels within the landslide, and (iii) geometric shadows cast within the landslide. We test these methods on three inventories of landslides of known timing, covering various settings and triggers, and demonstrate that, when used in combination, our methods allow 20% of landslides to be timed with an accuracy of 80%. This will allow multi-temporal landslide inventories to be generated for long rainfall events such as the Indian summer monsoon, which triggers large numbers of landslides every year and has until now been limited to annual-scale analysis.

1 Introduction

Every year, many mountainous areas in tropical zones are affected by destructive rainfall-induced landslide events that pose a major risk to people and infrastructure (Petley, 2012). With the advent of Earth observation from space, inventories of these landslides are routinely compiled from optical and multi-spectral satellite imagery (e.g., Marc et al., 2018; Emberson et al., 2021). These data are then used to provide information to emergency response coordinators, as inputs to physical and empirical models, and to assess the impact the event has had on the landscape, for example by estimating the volume of sediment eroded.

Landslide early warning systems, susceptibility zonation maps, nowcasts and hazard scenarios use information on the size location and timing of past landslides alongside information on the landscape conditions and triggering event (Guzzetti et al., 2020). While optical satellite imagery provides information on the size and location of landslides, cloud-free, daylight images are required. In unfavourable weather conditions, there may be a delay of weeks or months before cloud-free imagery over

the whole area affected by triggered landslides is acquired (Williams et al., 2018; Robinson et al., 2019). This means that the

25   timing of the landslides is often poorly constrained by the optical satellite imagery. In practice, this strongly limits or simply prevents any attempt to relate landslide metrics and hydrometeorological metrics resulting from successive or long rainfall events, whether through empirical scalings (e.g., Marc et al., 2018, 2019b) or physical modeling (e.g., Wilson and Wieczorek, 1995; Baum et al., 2010). In many tropical settings, multiple successive typhoons are common, for example typhoons Nesat, Haitang and Talim, which made landfall within a 2-month period in 2017 in Taiwan (Janapati et al., 2019). If no cloud-free

30   optical satellite imagery is acquired between these trigger events, the relationship between the hydrological impact of the storms and the triggered landslides cannot be precisely established. Similarly, the Indian summer monsoon (June-September) triggers hundreds of landslides every year in the Nepal Himalaya and cloud-free optical satellite imagery is unlikely to be available throughout this period (Robinson et al., 2019). This limits analysis of these landslides to the annual scale (e.g. Marc et al., 2019a; Jones et al., 2021).

35   Current alternative methods of landslide timing are generally not widely applicable. Landslides that occur close to inhabited areas, or that damage important pieces of infrastructure may be described in news reports or on social media (e.g., Kirschbaum et al., 2010). Information on the timing of such landslides can also be obtained from interviews with local residents (Bell et al., 2021). Rainfall intensity-duration thresholds have previously been derived for landslides dated in this way (e.g. Dahal and Hasegawa, 2008) and for landslides whose timings and properties are known through monitoring and field surveys (e.g.

40   Guzzetti et al., 2007; Ma et al., 2015). However this is unlikely to be the case for the majority of landslides in an inventory, and will be biased towards populated areas. Seismic records of landslides can also provide highly precise information on their timings, but will mostly record large landslides and require multiple seismic stations to allow timing of an individual, localised landslide (e.g. Yamada et al., 2012; Hibert et al., 2019).

    Regularly acquired synthetic aperture radar (SAR) images, for example those acquired by the European Space Agency

45   (ESA) Sentinel-1 constellation, represent a new opportunity to obtain landslide timing information for many landslides at regional scale. SAR images penetrate cloud cover and the Sentinel-1 satellites acquire images every 12 days on two tracks over all land masses globally. Numerous studies have demonstrated that SAR data can be used to detect the spatial distribution of landslides in the case where their timing is already known (Aimaiti et al., 2019; Burrows et al., 2019, 2020; Ge et al., 2019; Konishi and Suga, 2019; Masato et al., 2020; Mondini et al., 2021; Yun et al., 2015), for example in the case of earthquake-

50   triggered landslides where it can be assumed that the landslides occurred concurrently with ground shaking. SAR can be also used to monitor movements of slow-moving landslides (e.g. Ao et al., 2020; Bekaert et al., 2020; Hu et al., 2019; Kang et al., 2021; Solari et al., 2020). Mondini et al. (2019) used SAR to establish the timing of a single large landslide. However, to-date SAR has not been used to refine timing estimates of seasonal landslide inventories. Here we present methods of accomplishing this using Sentinel-1 SAR time series in Google Earth Engine. This will greatly improve the temporal resolution of

55   optically-derived landslide inventories and unlock new comparisons between measured or modelled hydrological time series and landslide occurrence.

2 Data and Methods

In order to obtain timed landslide information for inventories associated with long or successive rainfall events, we propose a two-step process, whereby landslide locations are mapped as polygons using optical satellite imagery, and the timings of individual landslides are then obtained from SAR time series. In this paper we address the second of these steps. We use Sentinel-1 time series over inventories of landslides whose timings are already known to test three potential landslide timing methods individually and in combination.

2.1 Case study events

We used three published polygon inventories of landslides whose timings are known a-priori to test and develop landslide timing methods. We filtered each inventory to remove landslides smaller than 2000 m^2, so that each landslide was expected to contain a minimum of 20 10 × 10 m SAR pixels. All three inventories are located in vegetated areas, which is generally the ideal condition for widespread landslide mapping based on multi-spectral satellite imagery.

We used two inventories of landslides from Emberson et al. (2021) triggered by short rainfall events, whose timing is therefore known to within a few days. First, an inventory of 543 landslides triggered in Hiroshima, Japan by a heavy rainfall event which took place from 28 June to 9 July 2018, which were mapped using a combination of drone and aerial imagery (inventory from The Association of Japanese Geographers, 2019). The majority of landslides triggered by this event are believed to have occurred during peaks in rainfall intensity on the 6-7 July (Hashimoto et al., 2020). Second, we used an inventory of 383 landslides triggered by Cyclone Idai in Zimbabwe between 15-19 March 2019. This inventory was compiled as part of the study of Emberson et al. (2021) using Planetdove optical satellite images acquired on 20 and 24 March. Media reports on this event suggest that the majority of landsliding occurred between the 15-17 March (BBC News, 2019; Ministry of Information and Broadcasting, 2019; OCHA, 2019).

The third inventory used to test our methods is that of Roback et al. (2018) compiled for the M_w 7.8 Gorkha, Nepal earthquake, which occurred on 25 April 2015. The Nepal Himalaya is an area which experiences long periods of cloud cover and large numbers of rainfall-triggered landslides annually due to the monsoon and the country's steep topography. It is therefore useful to test landslide timing methods in this area, and, since well-timed rainfall-triggered landslide information is not widely available, we used earthquake-triggered landslides, which can be assumed to occur concurrently with the ground shaking. Since the inventory of Roback et al. (2018) covers a large area, with different areas having different Sentinel-1 coverage, we focussed on triggered landslides within three large valleys: Trishuli , Bhote Kosi and Buri Gandaki. These valleys see large numbers of rainfall-triggered landslides every year, the timing of which would be one of the key applications of our method (Marc et al., 2019a). The M_w 7.8 mainshock on 25 April was followed by other possible landslide triggers, including the M_w 7.3 Dolakha aftershock on 12 May as well as the annual monsoon, whose onset was around 9 June (Williams et al., 2018). Therefore for this inventory, as well as filtering by landslide area, we also removed all landslides whose trigger was specified by Roback et al. (2018) to be something other than the mainshock. This left 650 landslides in Trishuli, 1554 in Bhote Kosi and 922 in Buri Gandaki. The Dolakha aftershock is known to have triggered further landsliding (see Marc et al., 2019a). However of the three
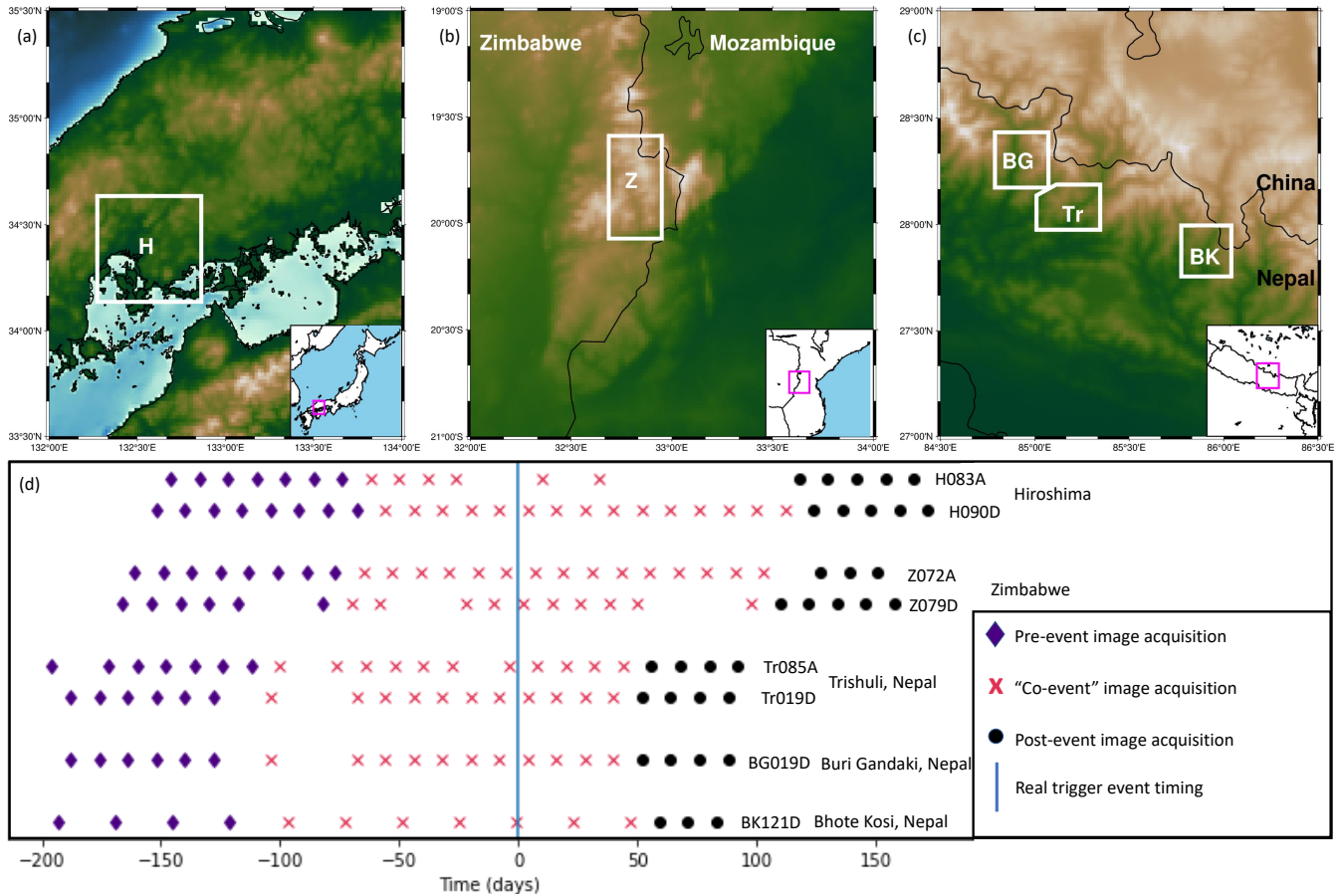
Figure 1. (a-c) locations of the five inventories of triggered landslides used in this study to test landslide timings. (d) SAR image acquisition timings before, during and after a defined "co-event" window of 6 months relative to the real event timing.

valleys we consider here, only Bhote Kosi was close enough to the epicentre to be affected by that event (Martha et al., 2017). Since the co-event pair of SAR images for Bhote Kosi (24 April - 18 May 2015) spans both the Gorkha earthquake on 25 April and the Dolakha aftershock on 12 May, these two earthquakes can be considered as a single triggering event in Bhote Kosi.

2.2 Theory: SAR backscatter and landslides

A SAR satellite actively illuminates the Earth's surface with microwave energy, and records the phase and amplitude of the returned signal. The difference in phase between two images acquired over the same area at different times can be used to track the movement of the Earth's surface, for example movement on a fault during an earthquake, while the amplitude describes the strength of the backscattered SAR signal. The power of the signal transmitted P_r and received P_t by the sensor are described by Eq. 1, where λ is the wavelength, G^2 is the two-way antenna gain and R is the slant range (Small et al., 2004).

$$\overline{P_r} = \frac{\lambda^2}{(4\pi)^3} \int_{Area} \frac{P_t G^2 x^0}{R^4} dA \tag{1}$$

100   This equation is solved to obtain x^0, the backscatter coefficient, which can be either σ^0, γ^0 or β^0 depending on whether the integration is carried out in the ground (ellipsoid) plane, the plane perpendicular to the look direction or the slant-range plane respectively (Small et al., 2004). Different studies have demonstrated that all three of these backscatter coefficients can be applied to detect vegetation removal due to landslides and other processes such as deforestation and wildfires (e.g. Ban et al., 2020; Belenguer-Plomer et al., 2019; Bouvet et al., 2018; Esposito et al., 2020; Hernandez et al., 2021; Konishi and Suga,

105   2018; Mondini, 2017; Mondini et al., 2019; Motohka et al., 2014). Here we used γ^0.

    SAR backscatter is dependent on a number of factors, including the polarisation and wavelength used by the SAR system, the local slope orientation relative to the SAR sensor and the roughness and dielectric properties (e.g. soil moisture, presence of vegetation) of the material that the microwave energy interacts with at the Earth's surface. Sentinel-1 acquires C-band SAR data with a wavelength around 5.5 cm in two polarisations: "VV" (vertical polarisation) and "VH" (cross polarisation). We

110   tested both of these polarisations, but found VV to perform better than VH so present only the results for VV. VV data have also been acquired more consistently throughout the lifetime of Sentinel-1 than VH. In general, for vertically polarised SAR images, rougher surfaces result in increased backscatter, as does increased soil moisture. However, the relationship between these properties and the SAR amplitude is not simple: roughness has a stronger effect in locations with a high incidence angle (Baghdadi et al., 2016; Dubois et al., 1995), while changes in soil moisture have a larger effect at low incidence angles

115   (Baghdadi et al., 2016).

    Landslides alter the local topography (and therefore the local incidence angle) of the landscape through the movement of material and remove vegetation, which alters the dielectric properties and roughness of the Earth's surface. For this reason, landslides can result in both increases and decreases in amplitude. In fact within a single landslide, the amplitude of some pixels may increase while some decrease (e.g. Tozang landslide, Mondini et al., 2021, Fig 4).

120   **2.3   SAR data and preprocessing**

To construct our SAR amplitude time series, we used the Google Earth Engine Sentinel-1 ground range detected (GRD) data set. These data are preprocessed following the workflow of Filipponi (2019) to obtain the σ^0 backscatter coefficient in geographic coordinates at a resolution of 20 x 22 m and a pixel size of 10 x 10 m. We then applied the module of Vollrath et al. (2020) using the SRTM 30 m digital elevation model (DEM) to carry out an angular radiometric slope correction based on the

125   volume scattering model of Hoekman and Reiche (2015). This has the effect of converting from σ^0 (normalised in the ellipsoid plane) to γ^0 (normalised in the plane perpendicular to local satellite look direction). The aim of this step is to reduce the effects of topography on the SAR backscatter. In preliminary testing, we found that γ^0 performed better than σ^0. The module of Vollrath et al. (2020) also provides a shadow and layover mask that can be used to remove areas that are not well-imaged by the satellite due to the viewing angle and local topography. This masking step is important for landslide studies as they are

130   likely to be carried out in areas of steep topography.

For each of our three events, we defined a "co-event" period of approximately six months. We also defined a three-month pre-event period and two-month post-event period immediately before and after the co-event window. These pre-event and post-event image stacks are required in some of the methods outlined in Sect. 2.

The dates that make up the pre-event, "co-event" and post-event time series for each case study are shown in Fig. 1d.

135 The length of the "co-event" period was defined as 6 months for the Hiroshima and Zimbabwe events. For the three Nepal inventories, this was reduced to 5 months in order to allow a sufficient pre-event images to be acquired following the satellite launch in 2014 and sufficient post-event images to be acquired before the end of July, since few Sentinel-1 images are available over Nepal in August, September and October 2015. Unfortunately, insufficient data were acquired on the ascending orbit over BG and BK, so we only present results based on the descending track data for these two inventories. In this figure

140 and throughout the manuscript, we refer to SAR data according to the event, track number and orbit direction, for example, ascending track 72 over Zimbabwe will be referred to as Z072A. Any date for which SAR imagery only covered part of the inventory was omitted from the time series.

2.4 SAR amplitude techniques for landslide timing

2.4.1 Method 1: Landslide-background difference

145 We expect a landslide to result in a permanent change in an amplitude time series. However, factors other than landslides can also result in amplitude change. In particular, the rainfall that triggers the landslides will alter the soil moisture content and so may also alter the amplitude of the returned signal. To overcome this, we calculate a background amplitude signal for each landslide. First, we calculated a buffer region between 30 and 500 m around each landslide (Fig. 2a). Then we filtered this buffer to remove any pixels that lie within other landslide polygons and pixels that are dissimilar to those within

150 the landslide, for example pixels located on the opposite side of a ridge, in a river or with different surface cover. In order to assess pixel similarity we calculated three surfaces from pre-event satellite imagery. First, we calculated the normalised difference vegetation index (NDVI) from a single pre-event Sentinel-2 (or, where this was unavailable, Landsat-8) image for each event. Pixels with similar NDVI values are expected to have similar land-cover. Second, we used a stack of N pre-event SAR images i (Fig. 1) to calculate the mean amplitude $A_{mean,j}$ (Eq. 2) and amplitude variability $\Delta A_{mean,j}$ (Eq. 3) for every

155 pixel j through time. Pre-event amplitude and amplitude variability have previously been used by Spaans and Hooper (2016) to identify statistically similar pixels in SAR images.

$$A_{mean,j} = \frac{1}{N} \sum_{i=1}^{N} A_{i,j} \tag{2}$$

$$\Delta A_{mean,j} = \frac{1}{N} \sum_{i=1}^{N} (A_{mean,j} - A_{i,j}) \tag{3}$$
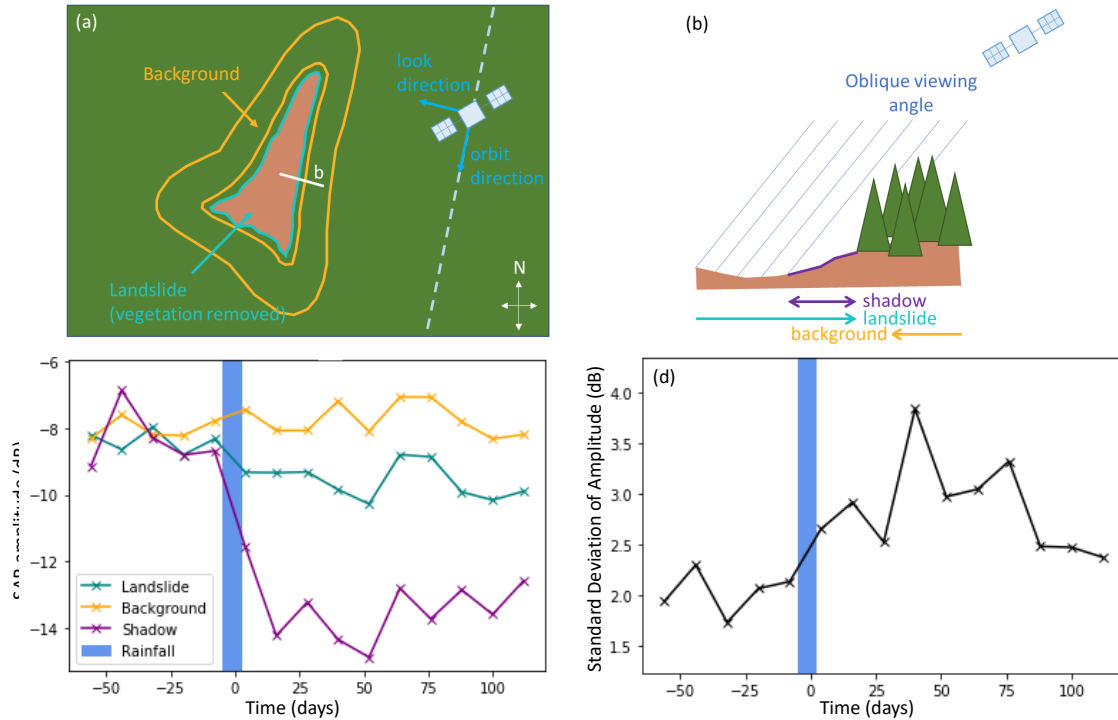
Figure 2. (a,b) Plan and lateral views of a landslide and satellite, showing how background and shadow regions are formed in this study. (c,d) Example time series for a single landslide from the Hiroshima dataset using SAR data from Sentinel-1 track 090D. Blue bar shows the duration of the rainfall event during which the landslide was triggered. (c) The median SAR amplitude for the landslide, the local background signal and areas of geometric shadow. (d) SAR amplitude standard deviation for pixels within the landslide

For every landslide, we calculated the range of NDVI, $A_{mean,j}$ and $\Delta A_{mean,j}$ values seen within the polygon. The buffer of

160 this landslide was then filtered to remove pixels with values outside these ranges. From this filtered buffer, we then calculated the median background amplitude for every image in the co-event time series. A step change in the difference between the median landslide amplitude and the median background amplitude is then used as an indicator of landslide timing. As previously described, landslides can result in both increases and decreases in SAR amplitude. When combining methods, we found that using the increase and decrease in amplitude as separate inputs resulted in better performance than combining these into a

165 single input, for example based on the absolute change in amplitude. Therefore, for this method, we accept both a step increase and a step decrease as a potential indicator of landslide timing.

2.4.2 Method 2: Pixel variability

Ban et al. (2020) observed that in forested and grassland areas, the removal of vegetation due to forest fires led to an increase in the variability of vertically polarised Sentinel-1 γ_0 between neighbouring pixels. Since landslides result in a similar denudation of vegetated areas, we expect that similar effects may occur. Therefore, we calculated the standard deviation of γ^0 within each landslide polygon and used a step increase in this as a potential indicator of landslide timing (e.g. Fig.2d).

2.4.3 Method 3: Geometric shadows

Since SAR is acquired obliquely (with an ellipsoid incidence angle of 31-44 ° for the data used here), steep changes in scatterer surface height can result in geometric shadows. The wavelength of Sentinel-1 means that is primarily scattered from the canopy in forested areas, which means that shadows can be cast at the edges of deforested areas if these edges run approximately perpendicular to the satellite look direction (Fig. 2b). Bouvet et al. (2018) developed a method for automatically detecting deforested areas based on these geometric shadows. Since landslides remove vegetation, we expect that shadows should also be cast at the edges of landslides, and that the appearance of new shadows could be used as an indicator of landslide timing. Furthermore, the three-dimensional shape of the landslide could result in shadows cast within the landslide itself, for example if the landslide has a steep scar. This effect has previously been observed within a large landslide in Nepal by Ao et al. (2020). It is worth noting that, while Bouvet et al. (2018) applied their methods in areas of gentle slopes, the area of a shadow cast by an object of a given height is dependent on slope and aspect: trees of the same height will cast a larger shadow on slopes facing away from the sensor than on those facing towards it. Therefore, we expect this method to be more successful for slopes that face away from the sensor.

In comparisons of multiple inventories of the same event prepared by different people or groups, there are often small discrepancies in the exact size, shape and location of each landslide (Milledge et al., 2021; Pokharel et al., 2021). Since shadow pixels are most likely to lie at the edges of the landslide polygons, it is important not to exclude the edge of a landslide from the analysis. Therefore we extended the area covered by each landslide polygon by 10 m (one SAR pixel) where this did not lead to intersection with another landslide in the inventory. We then identified pixels whose amplitude decreased within this enlarged polygon as shadows. Bouvet et al. (2018) identified shadow pixels as those whose γ_0 value decreased by >= 4.5 dB during the deforestation event. We tested values between 3 and 6 dB and also found that a threshold of 4.5 dB performed best. We calculated the mean γ_0 value for every pixel from the pre-event and post-event image stacks and assigned those that decreased by >= 4.5 dB as shadow pixels. The co-event time series of these shadow pixels was then analysed and a step decrease in the median shadow γ_0 relative to the median background γ_0 (Sect. 2.4.1) was used as an indicator of landslide timing.

2.5 Step change identification

For every landslide, the step change in the landslide timing indicators described in Sects. 2.4.2, 2.4.1 and 2.4.3 was identified by convolution with a step function. The step function was made up of a series of -1s and 1s of twice the length of the co-event

Table 1. Confusion matrix for determining how convolution peak size relates to whether a landslide timing is likely to be correct

	Peak synchronous with trigger event	Peak asynchronous with trigger event
Peak > threshold (dated)	True Positive	False Positive
Peak < threshold (masked)	False Negative	True Negative

time series. The landslide indicator time series had its mean value subtracted from it so that it is centred on 0. The two of these

200 were then convolved, resulting in a function where a peak indicates a step increase and a trough represents a step decrease in the landslide indicator time series.

The size of the peak or trough depends on the magnitude of the increase or decrease, the level of noise elsewhere in the time series and the length of the co-event time series (n_{dates}). A bigger peak or trough for a time series of the same length indicates a larger step change and less noise and is therefore a more reliable indicator of landslide timing. We therefore apply a peak size

205 threshold to remove unreliable landslide timing estimates. To select this threshold for each method, we use the F1-measure, a statistic that combines both precision and recall. This F1-measure was calculated for a range of peak thresholds using the confusion matrix defined in Table 1 (Fig. 3). Based on this, we require a peak of $0.4 \times n_{dates}$ for the Landslide-Background Method, $0.2 \times n_{dates}$ for the Pixel Variability Method and $0.75 \times n_{dates}$ for the Geometric Shadows Method. We also assessed whether the level of noise in the time series for each metric (estimated from the variability in pre-event and post-event time

210 series), could be used to indicate whether a timing estimate was likely to be correct, but found this to be less reliable than the convolution peak size.

3 Results

We used each method in Sect. 2 to assign landslide dates for the five case study areas described in Sect. 2.1. Not all landslides are assigned a date by every method, for example if no geometric shadows are cast within the landslide polygons. Table 2

215 shows the number of landslides assigned a date by each method and the percentage of these dates that were correct in each case. A baseline was calculated from $\frac{1}{n_{dates}}$: the percentage of landslides we would expect to be assigned the correct date by chance for a method with no skill. All three methods consistently perform better than this baseline.

3.1 Combining methods

To assess the methods in combination, we take whichever date is predicted the most often for every landslide. Since it is

220 not possible for both a step increase and a step decrease in the Landslide-Background Method to predict the same date, the maximum number of times the same date can be predicted is 3. The number of landslides assigned a date by at least 2 methods and by all 3 methods and the percentages of these that are correct is shown in Table 2. The strong reduction in number of timed landslides when going from an individual method to 2 and then 3 methods in combination underlines the fact that the nature
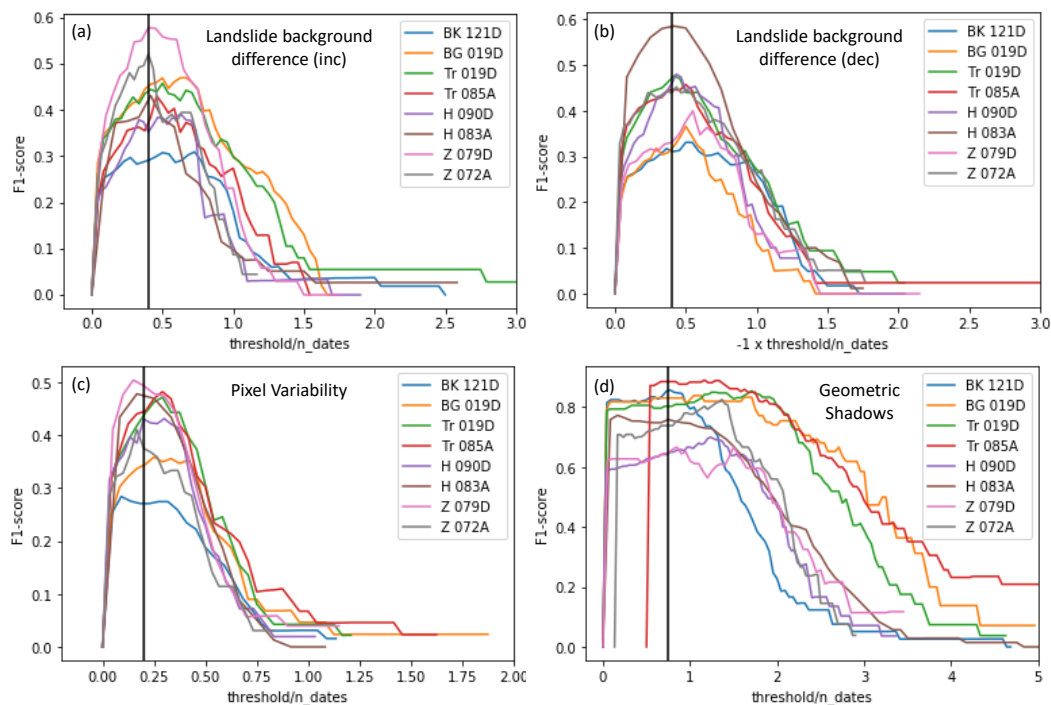
Figure 3. F1 scores for a range of peak thresholds for the Landslide-Background Method (a and b correspond to step increase and decrease respectively), the Pixel Variability Method (c) and the Geometric Shadows Method (d). Vertical black lines show selected thresholds.

of the change in amplitude varies widely between landslides. However, landslides dated by 2 or 3 methods are correctly dated
225 much more often. Across all 8 tracks, 56 landslides are predicted a date by 3 methods of which 52 (93%) are correct. Fig. 4
shows the number of times each date pair is predicted by $\geqslant 2$ methods and by 3 methods.

3.2 Combining tracks

Sentinel-1 acquires data on an ascending track, (moving northwards and looking east) and a descending track (moving south-
wards and looking west). Therefore, we can generate two sets of dates for each landslide inventory (excluding Bhote Kosi and
230 Buri Gandaki where only descending track SAR data were available). This has several advantages. First, landslides that were
not assigned a date using data from one track may be better dated by the second, increasing the number of landslides in the
inventory for which a date can be assigned. In particular, landslides that are masked due to foreshortening or layover in one
track may be better imaged in the other track. This was advantageous in Trishuli, where both ascending and descending tracks
were available and steep slopes meant that large numbers of landslides were masked in each case. 474 and 485 landslides
235 were imaged by the ascending and descending tracks respectively out of a possible 650 landslides in Trishuli. However, 516
landslides were imaged by at least one of the two tracks, thus coverage was improved by using both. Second, the acquisition
dates of the two tracks are slightly offset, so a landslide that is assigned a date by both tracks has a more precise timing. For

Table 2. For each case study, the total number of landslides, the number that are masked due to foreshortening or layover in the SAR images and amplitude timing results. For each method and combination of methods, we give the number of landslides assigned a date followed in brackets by the percentage of these assigned dates that are correct (the specificity of each method). Where timings were combined from multiple methods (M) or tracks (T), the number of these is specified in brackets

| Track | Hiroshima | | Zimbabwe | | Trishuli | | Buri Gandaki | Bhote Kosi |
	H090D	H083A	Z079D	Z072A	Tr019D	Tr085A	BG019D	BK121D
Total Landslides	543		383		650		922	1554
Non-masked	543	540	383	383	485	474	592	894
Landslide-background inc	137 (26%)	92 (36%)	90 (50%)	66 (41%)	106 (38%)	107 (35%)	152 (36%)	313 (36%)
Landslide-background dec	126 (38%)	205 (57%)	182 (23%)	155 (34%)	156 (37%)	143 (33%)	113 (27%)	310 (32%)
Pixel Variability	160 (45%)	181 (59%)	134 (50%)	83 (47%)	141 (42%)	125 (44%)	141 (30%)	261 (43%)
Geometric Shadows	79 (49%)	122 (75%)	43 (55%)	58 (72%)	45 (80%)	50 (80%)	17 (88%)	52 (87%)
Combined (≥ 2M)	51 (75%)	99 (88%)	48 (65%)	39 (85%)	45 (76%)	33 (88%)	33 (64%)	86 (63%)
Combined (3M)	10 (80%)	22 (100%)	5 (80%)	2 (50%)	8 (100%)	3 (100%)	1 (100%)	5 (100%)
Asc & Desc (Total)	122 (80%)		81(73%)		70 (81%)		-	-
Asc & Desc (2M, 1T)	79 (73%)		64 (72%)		52 (77%)		-	-
Asc & Desc (≥ 3M)	43 (91%)		17 (76%)		18 (94%)		-	-
Baseline (1/n_{dates})	7%	17%	10%	7%	8%	8%	8%	14%

example, a landslide in the Zimbabwe inventory should be dated as 7-19 March 2019 by the descending track time series and 12-24 March 2019 by the ascending track time series. From both of these together, the landslide would be dated as 12-19 March 2019, improving the precision from 12 days to 7. This more precise date is also more likely to be correct since it is derived from two sets of independent observations of the landslide.

For each event, we used the ascending and descending tracks to generate dates predicted by at least 2 methods on the same track. Out of all the non-masked landslides in each inventory, 23% were assigned a date in Hiroshima, 21% in Zimbabwe and 14% in Trishuli and of these, 80% of the estimated dates in Hiroshima were correct, 73% in Zimbabwe and 81% in Trishuli (Table 2). As well as being dated by 2 methods on the same track, a small number of landslides were dated either by the 3rd method on that track or by at least one method on the other track. These landslides whose dates were assigned based on 3 or more methods ("≥ 3M" in Table 2) were assigned the correct date more often than those assigned a date only based on 2 methods on one track ("2M, 1T" in Table 2). We also tested the case where landslides were dated based on the same date being selected by one method from each track, but found that this yielded too many incorrect dates to be useful.

3.3 Factors affecting performance of each method.

We assessed the performance of our dating methods as a function of the landslide characteristics, in terms of pre-event vegetation, landslide area, and slope aspect. This may inform future application of our methods.
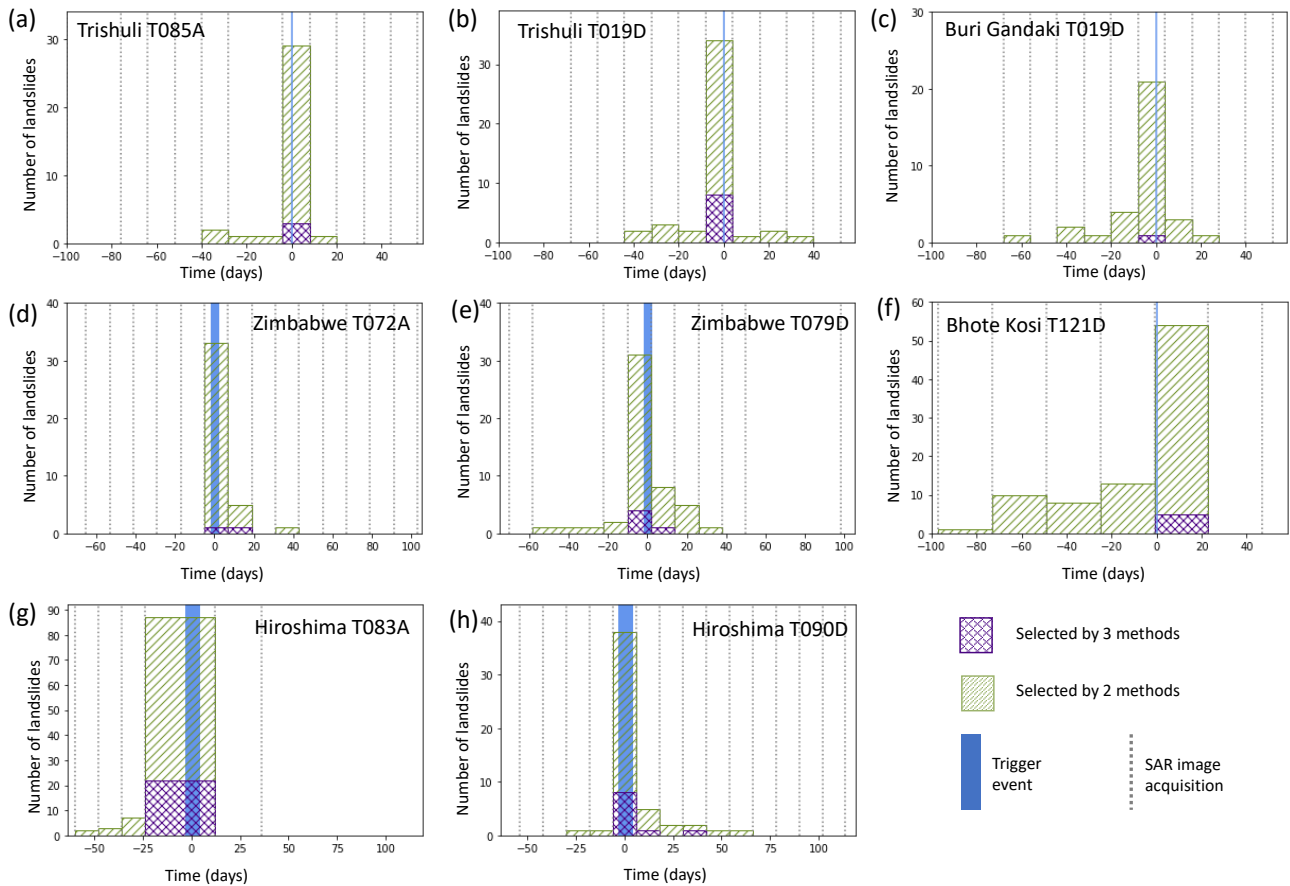
Figure 4. Histograms showing the predicted landslide timings for each event when three methods are used in combination.

3.3.1 Vegetation

In order to assess the effect that vegetation cover has on the methods we propose here, we compared the number of correctly
255 timed, incorrectly timed and untimed landslides with different values of pre-event NDVI (Fig. 5 a-c). We took the maximum
NDVI value for each pixel in the year preceding the event and used Sentinel-2 data for Zimbabwe and Hiroshima and Landsat
8 for Trishuli. In all three inventories, the majority of mapped landslides occurred in vegetated areas ($0.6 < NDVI < 0.8$). In
all three cases, a landslide in a more vegetated area was more likely to be assigned a date and this date was more likely to be
correct.
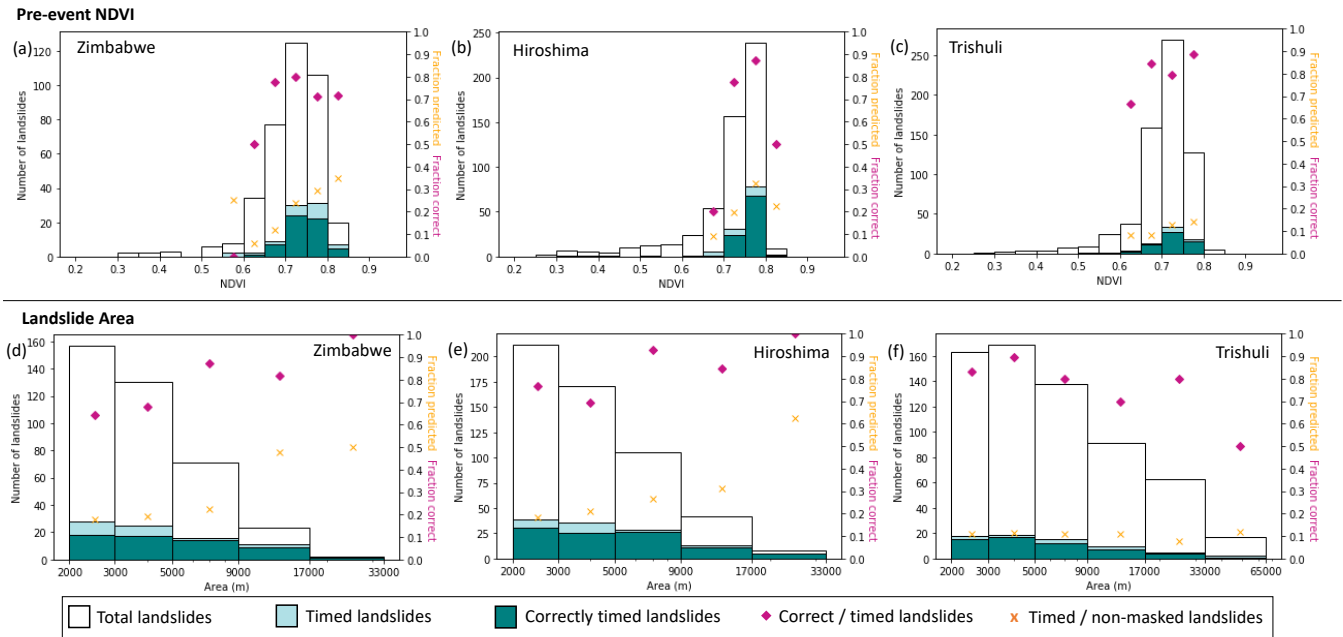
Figure 5. The distribution of total landslides (white), landslides assigned a time (light green) and landslides assigned the correct time (dark green) for different values of pre-event NDVI (greenest value in the year preceding the event, a-c) and landslide area (d-f). Predictions were obtained from combining ascending and descending track SAR (Sect. 3.2).

3.3.2 Area

Another factor that could potentially effect the applicability of the methods we present here is landslide area. Fig. 5d-f shows the distribution of landslides against landslide area. In Zimbabwe and Hiroshima, a higher proportion of larger landslides were assigned a date and a higher proportion of these assigned dates were correct, but these effects were not observed in Trishuli. We limited our testing to landslides whose area was greater than 2000 m^2. Since our methods rely on landslides containing multiple SAR pixels in order to calculated the statistics such as the standard deviation, there is likely to be a lower limit on the area of landslides that can be timed that was not reached here.

3.3.3 Aspect

The effect of aspect on landslide timing ability is more complicated than that of vegetation and area, since it is likely to vary between the ascending and descending track SAR. Therefore, in Fig. 6, we show the ascending and descending track predictions for each method for Zimbabwe (results are similar for Hiroshima and Trishuli). The different methods we propose in Sect. 2 have different relationships with aspect. For the Landslide-Background Difference Method, it appears that landslides on slopes facing towards the sensor are more likely to experience a step increase, while slopes facing away from the sensor are more likely to experience a step decrease. For the Pixel Variability Method, aspect does not appear to have a strong effect on

275 how likely a landslide is to be assigned the correct time. For the Geometric Shadows Method, a higher proportion of landslides are assigned a date (and therefore exhibit a shadow) on slopes facing away from the sensor. This was expected since the same height difference will cast a larger shadow on a slope facing away from the sensor than one facing towards it (Bouvet et al., 2018). Dates assigned by the Geometric Shadows Method also appear more likely to be correct for slopes facing away from the sensor on Z072A, but this pattern is less clear on Z079D.

4 Discussion

280 4.1 Possible causes of incorrect landslide timings

In all of our case studies, our methods assign the wrong dates to small number of landslides. There are several possible reasons for this. There may be real changes in the time series that are not landslides, for example snowfall or melt, change in vegetation, change in soil moisture or human activity, which may be related to the landslide, for example the removal of material from a blocked road. Random noise in the SAR signal may also result in false landslide timings. We note that for future applications, 285 the timing confidence within a landslide population can be separated into landslides timed by 3 or more methods and those timed by only 2 methods (Table 2)

Another possibility is that delayed or multi-stage failure occurred for some landslides. Our methods are designed to detect only a single failure. In the case where multi-stage failure results in more than one step change in the time series, the convolution in Sect. 2.5 will detect only the largest step change. Though it is beyond the scope of this study, it is in theory possible to assess 290 if the time-series contain a second peak, of similar magnitude to the largest one, to assess the likelihood of multistage failure or landslide reactivation.

Delayed failure seems particularly likely for Zimbabwe and Hiroshima, where a large proportion of the incorrect landslide timings are made up of the date pair immediately after the rainfall event (Fig. 4d, e, h). It is possible that some of the landslides in these inventories did not fail immediately during the rainfall, but instead failed after a delay of a few days due to rising pore 295 pressure following rainfall infiltration within the hillslope (Iverson, 2000). This is particularly possible in the case of Z079D, where the end of the rainfall event on 19 March 2019 coincides with the acquisition of the first post-event image, so that only a short delay would be required for the landslide to occur during the time window immediately after the rainfall (19-31 March 2019) rather than during the time window that spans the rainfall (7-19 March 2019). If these landslides are counted as correct in our analysis, the combined success rate in Zimbabwe is increased from 73% to 81%, bringing it in line with Hiroshima and 300 Trishuli (Table 2), while for landslides timed by 3 or more methods ("⩾3M" in Table 2), the success rate is increased from 76% to 94%.

Although the Gorkha earthquake was followed by a large aftershock (12 May) and by the monsoon (approximate onset 9 June) (Williams et al., 2018), we are more confident of the true date of the landslides for this event. It is possible that some landslides could have been either triggered or reactivated by monsoon rainfall. However, none of the incorrect landslide timings 305 in Nepal are in June, making this unlikely (Fig. 4a-c,f).
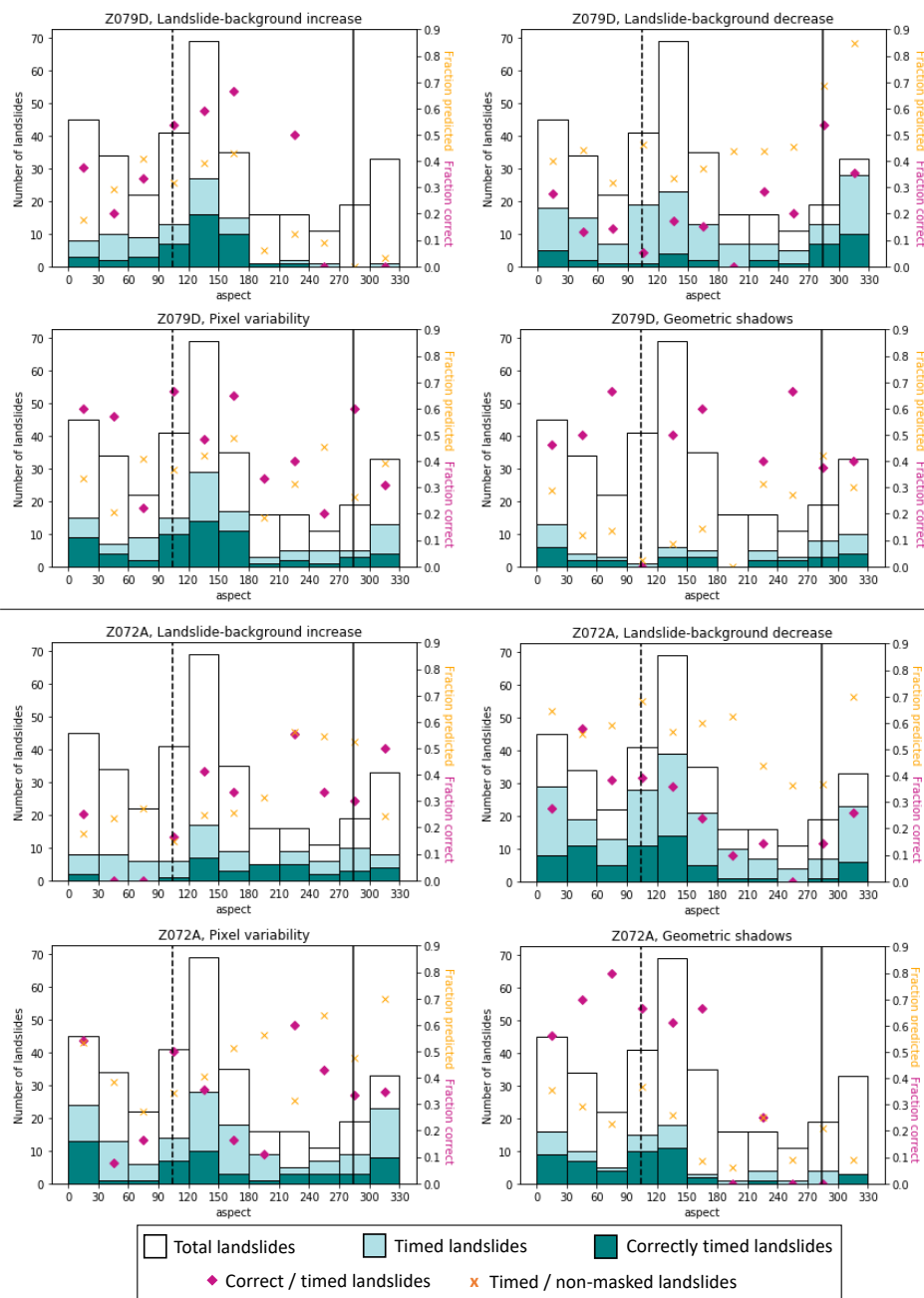
Figure 6. The distribution of total landslides (white), landslides assigned a time (light green) and landslides assigned the correct time (dark green) over aspect. Solid, black vertical line shows the aspect facing directly away from the SAR sensor. Dashed line shows aspect facing directly towards the SAR sensor.

4.2 Why do some landslides have no timing estimation?

In all our case studies, a large proportion of landslides are not assigned any date by the amplitude methods. Some of these landslides, primarily in Nepal, lie in areas of foreshortening or layover in the SAR images and so were removed from the analysis (Sect. 2.3). Beyond this, there are several reasons that landslides may not be assigned a timing.

310 In Sect. 2.5, we discarded predictions for which the peak was too small in our convolution function. This improved the specificity of our methods, but also required some correct predictions to be discarded. The reason for a small peak in the convolution function is either that the step change in the metric was too small, or the rest of the time series was too noisy. In Sect. 3.3, we demonstrated that landslides are less likely to be assigned a date if they occur in less vegetated areas or on slopes unfavourably oriented towards the sensor. This means that using SAR to detect landslides in arid areas remains a challenge,

315 although methods based on coherence time-series may be more appropriate in such cases (e.g. Cabré et al., 2020). In the case of the Geometric Shadows Method, there is no guarantee that a landslide will contain any shadow pixels, in which case no date can be detected using this method. This was observed to be more likely on slopes facing away from the sensor (Fig. 6).

Landslides will also have no signal in our methods if they are not located correctly in the SAR image, either due to distortion of the radar image or to inaccuracies in the optically-derived inventory. Milledge et al. (2021) and Pokharel et al. (2021)

320 both observed differences in landslide shape and location when comparing different optically-derived inventories of landslides triggered by the Gorkha earthquake, including the inventory of Roback et al. (2018) used here. Milledge et al. (2021) observed low spatial agreement between different inventories for all five of the trigger events they examined, suggesting this effect to be relatively common. Such differences can be due to problems georeferencing the optical imagery, imagery from different sources being used to compile different inventories and different teams of people carrying out the mapping. The landslide

325 timing methods we present here require precise landslide locations. For the Geometric Shadows Method, which we expected to be particularly sensitive to this form of spatial disagreement, we expanded the area covered by each landslide polygon by 10 m in an attempt to address this. However any mismatch beyond this scale between the landslide inventory and the SAR images is likely to lead to landslides not being assigned a timing.

4.3 The effect of shortening the time window

330 We used a "co-event" window of 6 months when testing the landslide timing methods in this paper. This time period was selected to be roughly the duration of the Nepal monsoon. However, some applications, for example the case of successive storms, may not require such a long window. It is therefore useful to assess how the length of this time window affects the accuracy of predictions. In order to assess this, we took the tracks with the most complete time series (Z072A, H090D, Tr019D and BG019D) and assessed their performance over 2-8 month periods. Fig. 7 shows the percentage of assigned timings that are

335 correct based on at least 2 methods for each track at each time period.

On all three tracks, particularly BG019D and H090D, the accuracy decreased as the co-event period was decreased. This was especially observed for periods of less than 5 months. We suggest that noise may be less attenuated in a shorter time series, resulting in increased numbers of false positives. Therefore, when applying our methods to future events, we recommend
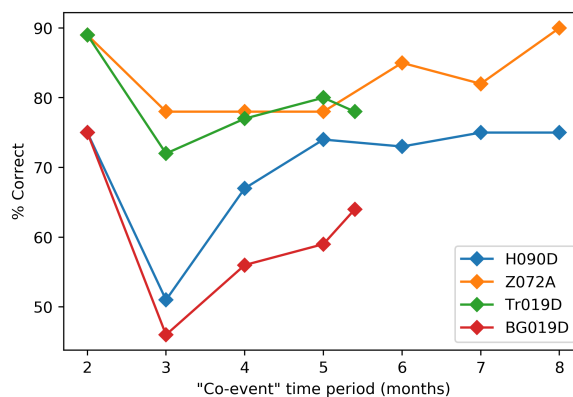
Figure 7. The percentage of landslide timings that are correct when assigned by $\geqslant 2$ of the methods described in Sect. 2.4 for a range of co-event time periods.

keeping a time window of at least 5 months even in the case where the landslide timing is known more precisely than this
340   beforehand. This may explain the relatively poor performance in Bhote Kosi compared to the other case study areas, since comparatively few images were available for this case study (Fig. 4). The loss of accuracy is recovered when the co-event period is further decreased to 2 months, possibly due to the comparatively small number of possible wrong date pairs available within a 2-month period.

4.4   InSAR Coherence

345   Interferometric SAR (InSAR) coherence is a measure of the signal quality of an interferogram (an image used to measure ground deformation formed from two SAR images acquired over the same area at different times). InSAR coherence is sensitive to changes at the ground surface between the acquisition of the two SAR images: areas where the scatterers have changed significantly have high levels of noise in an interferogram and so a low coherence. Coherence is therefore sensitive to landslides and has previously been used to detect landslide densities or individual large landslides (Burrows et al., 2019, 2020; Goorabi,
350   2020; Yun et al., 2015).

The coherence of each pixel in an interferogram can be estimated from the similarity in amplitude and phase change between the two SAR images for small groups of neighbouring pixels. Coherence surfaces and the phase data required for their calculation are not available through Google Earth Engine. However, coherence for Track 19 in Nepal has previously been calculated by Burrows et al. (2019), covering the Buri Gandaki and Trishuli inventories tested here. This allows us to compare methods
355   of landslide timing based on SAR amplitude and InSAR coherence for these two case studies.

Burrows et al. (2019) processed the data at the same resolution used here (20×20 m) and used a 3×3 moving window to estimate coherence, so that the coherence surface has a resolution of 60×60 m. Similarly to the Landslide-Background Method, we obtained the median coherence of pixels within each landslide through time and the median coherence of pixels
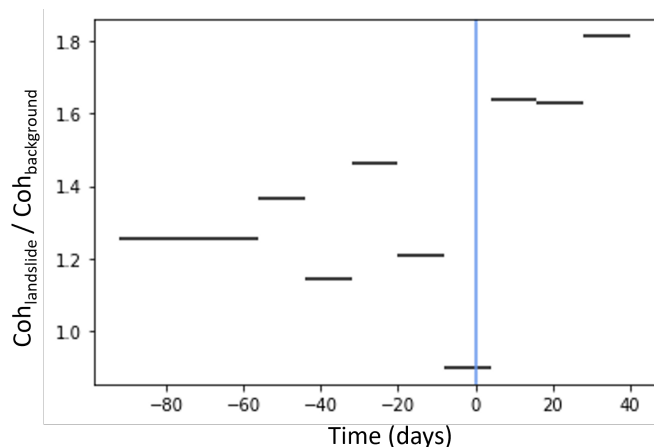
Figure 8. Time series of ratio between landslide coherence and background coherence for a single landslide in Trishuli (black horizontal lines). Blue vertical line shows earthquake timing.

.

within a 60-500 m buffer of each landslide polygon to give a background coherence. We then examined the ratio between the landslide and background coherence through time. Using this ratio performed better than using the landslide coherence alone, probably because other factors, such as the length of time between the two images used to form the interferogram, can also effect coherence. Fig. 8 shows the median coherence ratio of a single landslide for different image pairs through time. This demonstrates two effects that we expect to see. First, the coherence that spans the landslide timing is low. This drop in coherence has previously been used to detect landslide locations (Burrows et al., 2019; Goorabi, 2020; Yun et al., 2015). However Sentinel-1 often has a low background coherence in vegetated areas due to its wavelength, which can make any coherence decrease due to a landslide difficult to detect. Second, the coherence of post-event image pairs is higher than pre-event image pairs due to the removal of vegetation by the landslide (previously used by Burrows et al., 2020). Based on these two observations, we propose two landslide timing detection methods based on InSAR coherence time series.

Method C1: A step increase in the coherence ratio corresponds to the first post-event image pair.

Method C2: A temporary decrease in the coherence ratio corresponds to the co-event image pair. For each coherence pair, this temporary decrease is calculated from the sum of the decrease in coherence ratio from the previous image pair to this one and the increase in coherence ratio from this image to the next (adapted from the ΔC_sum method of Burrows et al., 2020).

Overall, the coherence-based methods have a lower success rate than the amplitude-based methods (Table 2), indicating that incorporating these data would decrease the specificity of our methods. However, it is worth noting that of the 47 landslides correctly timed across the two events using the C1 and C2 combined, only 3 had already been timed using the combined amplitude-based methods in Sect. 3.1, suggesting that the incorporation of coherence methods could increase sensitivity, if these could be made more reliable.

Table 3. The ratio of correct / assigned landslide timings for the two coherence-based methods

	Tr019D	BG019D
Method C1	54/154 (36%)	59/169 (35%)
Method C2	82/312 (26%)	96/396 (24%)
Combined	27/57 (47%)	20/56 (36%)
Non-masked landslides	485	592

Currently, only the Sentinel-1 SAR constellation acquires SAR data with sufficient coverage and acquisition frequency for use in landslide timing studies. These data are acquired at C-band, which usually has low coherence in vegetated areas. L-band data is better suited to InSAR-coherence-based landslide detection in vegetated areas (Burrows et al., 2020). The planned NASA-ISRO NISAR mission has a similar acquisition strategy to Sentinel and will acquire L-band SAR. It will be worth reassessing the potential of InSAR coherence time series for landslide timing detection following the launch of this satellite.

4.5   Application to future events

We have developed methods that allow around 20% of landslides in an inventory to be dated at the 6-12 days scale with $\sim 80\%$ confidence. In the case of multiple successive storms, this timescale should be sufficient to attribute landslides to a given event. For monsoon landslide dating, this timing is not sufficiently precise to allow building of intensity-duration or intensity-antecedent rainfall thresholds (e.g. Bogaard and Greco, 2018). However, it should allow us to establish whether landslides occur in temporal clusters that relate to specific peaks in rainfall or are distributed throughout the monsoon. These two end-members would have very different implications in terms of hydrological and slope stability modeling, and thus on hazard evaluation. It should also allow us to better constrain whether landslides systematically occur with a specific delay after the onset of the monsoon and/or simultaneously with reported flooding or bursts of intense rainfall (Gabet et al., 2004). In both cases, since relatively few landslides are timed by SAR methods, some inference will be needed to attribute time stamps to neighbouring landslides lacking a SAR signal. The SAR methods could also be combined with other methods of establishing landslide timing if these are available e.g. small gaps in cloud in optical satellite imagery, reports of individual landslides or seismic data (Bell et al., 2021; Hibert et al., 2019; Yamada et al., 2012).

An algorithm could be designed to automatically detect both the location and timings of rainfall-triggered landslides by combining SAR-based timing methods with automated landslide mapping methods based on multi-spectral imagery (e.g. Behling et al., 2014; Ghorbanzadeh et al., 2021; Jelének and Kopačková-Strnadová, 2021; Milledge et al., 2021). They could also be applied to other forms of landslide inventory, for example those based on LiDAR scans or high resolution optical images that allow landslide volumes to be estimated.

5 Conclusions

In the case of prolonged rainfall events, landslide inventories compiled from optical satellite imagery are often poorly constrained in time. Here we present methods of using Sentinel-1 SAR images in Google Earth Engine to identify the timing of rainfall triggered landslides to within a few days. We find that by combining ascending and descending track SAR, it is possible

405 to date $\sim 20\%$ of landslides in an inventory with an accuracy of $\sim 80\%$. A small number of landslides (3-8%) can be timed with accuracy of 90-95%. These methods will allow us to generate multi-temporal landslide inventories for long rainfall events, unlocking comparisons between rainfall data, hydrological models and triggered landsliding. It also suggests that SAR amplitude time-series could be combined with multispectral imagery in an algorithm aimed at detecting and mapping landsliding over regional scales.

410 *Code and data availability.* Sentinel-1 GRD and Sentinel-2 data are available open-access from ESA Copernicus and were accessed through Google Earth Engine (https://developers.google.com/earth-engine/datasets/catalog/sentinel, last access 19 Jan 2022). Images from the USGS Landsat archive were accessed through Google Earth Engine (https://developers.google.com/earth-engine/datasets/catalog/landsat, last access 19 Jan 2022). Landslide polygons were obtained from Roback et al. (2018) for Nepal (available at https://doi.org/10.5066/F7DZ06F9) and from Emberson et al. (2021) for Japan and Zimbabwe. Google Earth Engine and Python codes used in generating the time series and

415 detecting landslide timings will be provided if the manuscript is accepted for publication. Images were produced using Python Matplotlib (Hunter, 2007) and PyGMT (Uieda et al., 2021) software.

Author contributions. KB carried out data curation and analysis of the data and wrote the original draft of the manuscript. All authors were involved in reviewing and editing the manuscript and in developing the methodology.

Competing interests. The authors declare no conflict of interest.

420 *Acknowledgements.* KB is fund by a post-doctoral grant from the Centre National d'Études Spatiales (CNES): "Characterising the temporal evolution of rainfall-triggered landslides using radar and optical satellite data". We thank Robert Emberson for sharing some landslide inventories.

References

Aimaiti, Y., Liu, W., Yamazaki, F., and Maruyama, Y.: Earthquake-Induced Landslide Mapping for the 2018 Hokkaido Eastern Iburi Earth-
quake Using PALSAR-2 Data, Remote Sensing, 11, 2351, 2019.

Ao, M., Zhang, L., Dong, Y., Su, L., Shi, X., Balz, T., and Liao, M.: Characterizing the evolution life cycle of the Sunkoshi landslide in Nepal
with multi-source SAR data, Scientific reports, 10, 1–12, 2020.

Baghdadi, N., Choker, M., Zribi, M., Hajj, M. E., Paloscia, S., Verhoest, N. E., Lievens, H., Baup, F., and Mattia, F.: A new empirical model
for radar scattering from bare soil surfaces, Remote Sensing, 8, 920, 2016.

Ban, Y., Zhang, P., Nascetti, A., Bevington, A. R., and Wulder, M. A.: Near real-time wildfire progression monitoring with Sentinel-1 SAR
time series and deep learning, Scientific Reports, 10, 1–15, 2020.

Baum, R. L., Godt, J. W., and Savage, W. Z.: Estimating the timing and location of shallow rainfall-induced landslides using a model for
transient, unsaturated infiltration, Journal of Geophysical Research: Earth Surface, 115, F03 013, https://doi.org/10.1029/2009JF001321,
2010.

BBC News: Cyclone Idai: Zimbabwe school hit by landslide, https://www.bbc.com/news/world-africa-47602399, news report 17th March
2019, accessed 5th November 2021, 2019.

Behling, R., Roessner, S., Kaufmann, H., and Kleinschmit, B.: Automated Spatiotemporal Landslide Mapping over Large Areas Using
RapidEye Time Series Data, Remote Sensing, 6, 8026–8055, https://doi.org/10.3390/rs6098026, 2014.

Bekaert, D. P., Handwerger, A. L., Agram, P., and Kirschbaum, D. B.: InSAR-based detection method for mapping and monitoring slow-
moving landslides in remote regions with steep and mountainous terrain: An application to Nepal, Remote Sensing of Environment, 249,
111 983, 2020.

Belenguer-Plomer, M. A., Tanase, M. A., Fernandez-Carrillo, A., and Chuvieco, E.: Burned area detection and mapping using Sentinel-1
backscatter coefficient and thermal anomalies, Remote Sensing of Environment, 233, 111 345, 2019.

Bell, R., Fort, M., Götz, J., Bernsteiner, H., Andermann, C., Etzlstorfer, J., Posch, E., Gurung, N., and Gurung, S.: Major geomorphic events
and natural hazards during monsoonal precipitation 2018 in the Kali Gandaki Valley, Nepal Himalaya, Geomorphology, 372, 107 451,
2021.

Bogaard, T. and Greco, R.: Invited perspectives: Hydrological perspectives on precipitation intensity-duration thresholds for landslide initia-
tion: proposing hydro-meteorological thresholds, Natural Hazards and Earth System Sciences, 18, 31–39, 2018.

Bouvet, A., Mermoz, S., Ballère, M., Koleck, T., and Le Toan, T.: Use of the SAR shadowing effect for deforestation detection with Sentinel-1
time series, Remote Sensing, 10, 1250, 2018.

Burrows, K., Walters, R. J., Milledge, D., Spaans, K., and Densmore, A. L.: A new method for large-scale landslide classification from
satellite radar, Remote Sensing, 11, 237, 2019.

Burrows, K., Walters, R. J., Milledge, D., and Densmore, A. L.: A systematic exploration of satellite radar coherence methods for rapid
landslide detection, Natural Hazards and Earth System Sciences, 20, 3197–3214, 2020.

Cabré, A., Remy, D., Aguilar, G., Carretier, S., and Riquelme, R.: Mapping rainstorm erosion associated with an individual storm from
InSAR coherence loss validated by field evidence for the Atacama Desert, Earth Surface Processes and Landforms, 2020.

Dahal, R. K. and Hasegawa, S.: Representative rainfall thresholds for landslides in the Nepal Himalaya, Geomorphology, 100, 429–443,
2008.

Dubois, P. C., Van Zyl, J., and Engman, T.: Measuring soil moisture with imaging radars, IEEE transactions on geoscience and remote sensing, 33, 915–926, 1995.

Emberson, R., Kirschbaum, D. B., Amatya, P., Tanyas, H., and Marc, O.: Insights from the topographic characteristics of a large global catalogue of rainfall-induced landslide event inventories, Natural Hazards and Earth System Sciences Discussions, 2021.

Esposito, G., Marchesini, I., Mondini, A. C., Reichenbach, P., Rossi, M., and Sterlacchini, S.: A spaceborne SAR-based procedure to support the detection of landslides, Natural Hazards and Earth System Sciences, 20, 2379–2395, 2020.

Filipponi, F.: Sentinel-1 GRD preprocessing workflow, in: Multidisciplinary Digital Publishing Institute Proceedings, vol. 18, p. 11, 2019.

Gabet, E. J., Burbank, D. W., Putkonen, J. K., Pratt-Sitaula, B. A., and Ojha, T.: Rainfall thresholds for landsliding in the Himalayas of Nepal, Geomorphology, 63, 131–143, 2004.

Ge, P., Gokon, H., Meguro, K., and Koshimura, S.: Study on the Intensity and Coherence Information of High-Resolution ALOS-2 SAR Images for Rapid Massive Landslide Mapping at a Pixel Level, Remote Sensing, 11, 2808, 2019.

Ghorbanzadeh, O., Crivellari, A., Ghamisi, P., Shahabi, H., and Blaschke, T.: A comprehensive transferability evaluation of U-Net and ResU-Net for landslide detection from Sentinel-2 data (case study areas from Taiwan, China, and Japan), Scientific Reports, 11, 1–20, 2021.

Goorabi, A.: Detection of landslide induced by large earthquake using InSAR coherence techniques–Northwest Zagros, Iran, The Egyptian Journal of Remote Sensing and Space Science, 23, 195–205, 2020.

Guzzetti, F., Peruccacci, S., Rossi, M., and Stark, C. P.: Rainfall thresholds for the initiation of landslides in central and southern Europe, Meteorology and atmospheric physics, 98, 239–267, 2007.

Guzzetti, F., Gariano, S. L., Peruccacci, S., Brunetti, M. T., Marchesini, I., Rossi, M., and Melillo, M.: Geographical landslide early warning systems, Earth-Science Reviews, 200, 102 973, 2020.

Hashimoto, R., Tsuchida, T., Moriwaki, T., and Kano, S.: Hiroshima Prefecture geo-disasters due to Western Japan Torrential rainfall in July 2018, Soils and Foundations, 60, 283–299, 2020.

Hernandez, N. D., Pastrana, A. A., Garcia, L. C., de Leon, J. C. V., Alvarez, A. Z., Morales, L. D., Nemiga, X. A., and Posadas, G. D.: Co-seismic landslide detection after M 7.4 earthquake on June 23, 2020, in Oaxaca, Mexico, based on rapid mapping method using high and medium resolution synthetic aperture radar (SAR) images, Landslides, pp. 1–12, 2021.

Hibert, C., Michéa, D., Provost, F., Malet, J., and Geertsema, M.: Exploration of continuous seismic recordings with a machine learning approach to document 20 yr of landslide activity in Alaska, Geophysical Journal International, 219, 1138–1147, 2019.

Hoekman, D. H. and Reiche, J.: Multi-model radiometric slope correction of SAR images of complex terrain using a two-stage semi-empirical approach, Remote Sensing of Environment, 156, 1–10, 2015.

Hu, X., Bürgmann, R., Lu, Z., Handwerger, A. L., Wang, T., and Miao, R.: Mobility, thickness, and hydraulic diffusivity of the slow-moving Monroe landslide in California revealed by L-band satellite radar interferometry, Journal of Geophysical Research: Solid Earth, 124, 7504–7518, 2019.

Hunter, J. D.: Matplotlib: A 2D graphics environment, Computing in Science & Engineering, 9, 90–95, https://doi.org/10.1109/MCSE.2007.55, 2007.

Iverson, R. M.: Landslide triggering by rain infiltration, Water resources research, 36, 1897–1910, 2000.

Janapati, J., Seela, B. K., Lin, P.-L., Wang, P. K., and Kumar, U.: An assessment of tropical cyclones rainfall erosivity for Taiwan, Scientific reports, 9, 1–14, 2019.

Jelének, J. and Kopačková-Strnadová, V.: Synergic use of Sentinel-1 and Sentinel-2 data for automatic detection of earthquake-triggered landscape changes: A case study of the 2016 Kaikoura earthquake (Mw 7.8), New Zealand, Remote Sensing of Environment, 265, 112 634, 2021.

Jones, J. N., Boulton, S. J., Stokes, M., Bennett, G. L., and Whitworth, M. R.: 30-year record of Himalaya mass-wasting reveals landscape perturbations by extreme events, Nature communications, 12, 1–15, 2021.

Kang, Y., Lu, Z., Zhao, C., Xu, Y., Kim, J.-w., and Gallegos, A. J.: InSAR monitoring of creeping landslides in mountainous regions: A case study in Eldorado National Forest, California, Remote Sensing of Environment, 258, 112 400, 2021.

Kirschbaum, D. B., Adler, R., Hong, Y., Hill, S., and Lerner-Lam, A.: A global landslide catalog for hazard applications: method, results, and limitations, Natural Hazards, 52, 561–575, 2010.

Konishi, T. and Suga, Y.: Landslide detection using COSMO-SkyMed images: a case study of a landslide event on Kii Peninsula, Japan, European Journal of Remote Sensing, 51, 205–221, 2018.

Konishi, T. and Suga, Y.: Landslide detection with ALOS-2/PALSAR-2 data using convolutional neural networks: a case study of 2018 Hokkaido Eastern Iburi earthquake, in: Proc. of SPIE Vol, vol. 11154, pp. 111 540H–1, 2019.

Ma, T., Li, C., Lu, Z., and Bao, Q.: Rainfall intensity–duration thresholds for the initiation of landslides in Zhejiang Province, China, Geomorphology, 245, 193–206, 2015.

Marc, O., Stumpf, A., Malet, J.-P, Gosset, M., Uchida, T., and Chiang, S.-H.: Initial insights from a global database of rainfall-induced landslide inventories: the weak influence of slope and strong influence of total storm rainfall, Earth Surface Dynamics, 6, 903–922, 2018.

Marc, O., Behling, R., Andermann, C., Turowski, J., Illien, L., Roessner, S., and Hovius, N.: Long-term erosion of the Nepal Himalayas by bedrock landsliding: the role of monsoons, earthquakes and giant landslides, Earth Surface Dynamics, 7, 107–128, 2019a.

Marc, O., Gosset, M., Saito, H., Uchida, T., and Malet, J.-P.: Spatial patterns of storm-induced landslides and their relation to rainfall anomaly maps, Geophysical Research Letters, 46, 11 167–11 177, 2019b.

Martha, T. R., Roy, P., Mazumdar, R., Govindharaj, K. B., and Kumar, K. V.: Spatial characteristics of landslides triggered by the 2015 M w 7.8 (Gorkha) and M w 7.3 (Dolakha) earthquakes in Nepal, Landslides, 14, 697–704, 2017.

Masato, O., Abe, T., Takeo, T., and Masanobu, S.: Landslide detection in mountainous forest areas using polarimetry and interferometric coherence, Earth, Planets and Space (Online), 72, 2020.

Milledge, D. G., Bellugi, D. G., Watt, J., and Densmore, A. L.: Automated landslide detection outperforms manual mapping for several recent large earthquakes, Natural Hazards and Earth System Sciences Discussions, pp. 1–39, 2021.

Ministry of Information, P. and Broadcasting, Z.: https://twitter.com/InfoMinZW/status/1107121417773035521, tweet @infoMinZW, 17th March 2019, accessed 5th November 2021, 2019.

Mondini, A. C.: Measures of spatial autocorrelation changes in multitemporal SAR images for event landslides detection, Remote Sensing, 9, 554, 2017.

Mondini, A. C., Santangelo, M., Rocchetti, M., Rossetto, E., Manconi, A., and Monserrat, O.: Sentinel-1 SAR amplitude imagery for rapid landslide detection, Remote sensing, 11, 760, 2019.

Mondini, A. C., Guzzetti, F., Chang, K.-T., Monserrat, O., Martha, T. R., and Manconi, A.: Landslide failures detection and mapping using Synthetic Aperture Radar: Past, present and future, Earth-Science Reviews, p. 103574, 2021.

Motohka, T., Shimada, M., Uryu, Y., and Setiabudi, B.: Using time series PALSAR gamma nought mosaics for automatic detection of tropical deforestation: A test study in Riau, Indonesia, Remote Sensing of Environment, 155, 79–88, 2014.

OCHA: Cyclone Idai hits Zimbambe, causing flash flooding, death and destruction of livelihoods, https://www.unocha.org/story/cyclone-idai-hits-zimbambe-causing-flash-flooding-death-and-destruction-livelihoods, news report 17th March 2019, accessed 5th November 2021, 2019.

Petley, D.: Global patterns of loss of life from landslides, Geology, 40, 927–930, 2012.

Pokharel, B., Alvioli, M., and Lim, S.: Assessment of earthquake-induced landslide inventories and susceptibility maps using slope unit-based logistic regression and geospatial statistics, Scientific Reports, 11, 1–15, 2021.

Roback, K., Clark, M. K., West, A. J., Zekkos, D., Li, G., Gallen, S. F., Chamlagain, D., and Godt, J. W.: The size, distribution, and mobility of landslides caused by the 2015 Mw7. 8 Gorkha earthquake, Nepal, Geomorphology, 301, 121–138, 2018.

Robinson, T. R., Rosser, N., and Walters, R. J.: The spatial and temporal influence of cloud cover on satellite-based emergency mapping of earthquake disasters, Scientific reports, 9, 1–9, 2019.

Small, D., Meier, E., and Nuesch, D.: Robust radiometric terrain correction for SAR image comparisons, in: IGARSS 2004. 2004 IEEE International Geoscience and Remote Sensing Symposium, vol. 3, pp. 1730–1733, IEEE, 2004.

Solari, L., Del Soldato, M., Raspini, F., Barra, A., Bianchini, S., Confuorto, P., Casagli, N., and Crosetto, M.: Review of Satellite Interferometry for Landslide Detection in Italy, Remote Sensing, 12, 1351, 2020.

Spaans, K. and Hooper, A.: InSAR processing for volcano monitoring and other near-real time applications, Journal of Geophysical Research: Solid Earth, 121, 2947–2960, 2016.

The Association of Japanese Geographers: The 2018 July Heavy rain in West Japan, http://ajg-disaster.blogspot.com/2018/07/3077.html,[dataset], accessed on 1 November 2019, 2019.

Uieda, L., Tian, D., Leong, W. J., Jones, M., Schlitzer, W., Toney, L., Grund, M., Yao, J., Magen, Y., Materna, K., Newton, T., Anant, A., Ziebarth, M., and Quinn, Jamie aand Wessel, P.: PyGMT: A Python interface for the Generic Mapping Tools, https://doi.org/10.5281/zenodo.5607255, 2021.

Vollrath, A., Mullissa, A., and Reiche, J.: Angular-based radiometric slope correction for Sentinel-1 on google earth engine, Remote Sensing, 12, 1867, 2020.

Williams, J. G., Rosser, N. J., Kincey, M. E., Benjamin, J., Oven, K. J., Densmore, A. L., Milledge, D. G., Robinson, T. R., Jordan, C. A., and Dijkstra, T. A.: Satellite-based emergency mapping using optical imagery: experience and reflections from the 2015 Nepal earthquakes., Natural hazards and earth system sciences., 18, 185–205, 2018.

Wilson, R. C. and Wieczorek, G. F.: Rainfall Thresholds for the Initiation of Debris Flows at La Honda, California, Environmental & Engineering Geoscience, I, 11–27, https://doi.org/10.2113/gseegeosci.I.1.11, 1995.

Yamada, M., Matsushi, Y., Chigira, M., and Mori, J.: Seismic recordings of landslides caused by Typhoon Talas (2011), Japan, Geophysical Research Letters, 39, 2012.

Yun, S.-H., Hudnut, K., Owen, S., Webb, F., Simons, M., Sacco, P., Gurrola, E., Manipon, G., Liang, C., Fielding, E., et al.: Rapid Damage Mapping for the 2015 M w 7.8 Gorkha Earthquake Using Synthetic Aperture Radar Data from COSMO–SkyMed and ALOS-2 Satellites, Seismological Research Letters, 86, 1549–1556, 2015.